

InstantSplat: Sparse-view Gaussian Splatting in Seconds

Zhiwen Fan^{1,2†*}, Kairun Wen^{3*}, Wenyang Cong^{1*}, Kevin Wang¹, Jian Zhang³, Xinghao Ding³, Danfei Xu^{2,4}, Boris Ivanovic², Marco Pavone^{2,5}, Georgios Pavlakos¹, Zhangyang Wang¹, Yue Wang^{2,6}

*Authors contributed equally; † Z. Fan is the Project Lead.

¹University of Texas at Austin ²Nvidia Research ³Xiamen University

⁴Georgia Institute of Technology ⁵Stanford University ⁶University of Southern California

Project Website: <https://instantsplat.github.io>

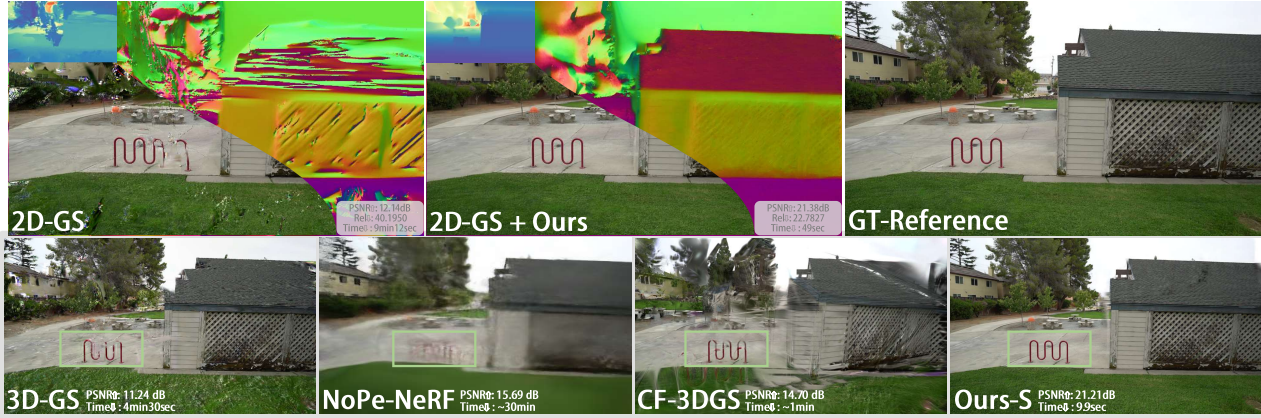


Figure 1. **InstantSplat** rapidly reconstructs a dense 3D model from sparse-view images. Instead of relying on traditional Structure-from-Motion poses and the complex adaptive density control strategy of 3D-GS[20], which is fragile under sparse-view conditions, we propose to synergize the geometric foundation model (i.e., MAST3R [22]) for dense yet less accurate initialization along with a fast alignment step to jointly optimize camera poses and the 3D scenes. It supports various 3D representations, including 2D-GS, 3D-GS, and Mip-Splatting.

Abstract

While neural 3D reconstruction has advanced substantially, its performance significantly degrades with sparse-view data, which limits its broader applicability, since SfM is often unreliable in sparse-view scenarios where feature matches are scarce. In this paper, we introduce **InstantSplat**, a novel approach for addressing sparse-view 3D scene reconstruction at lightning-fast speed. InstantSplat employs a self-supervised framework that optimizes 3D scene representation and camera poses by unprojecting 2D pixels into 3D space and aligning them using differentiable neural rendering. The optimization process is initialized with a large-scale trained geometric foundation model, which provides dense priors that yield initial points through model inference, after which we further optimize all scene parameters using photometric errors. To mitigate redundancy introduced by the prior model, we propose a

co-visibility-based geometry initialization, and a Gaussian-based bundle adjustment is employed to rapidly adapt both the scene representation and camera parameters without relying on a complex adaptive density control process. Overall, InstantSplat is compatible with multiple point-based representations for view synthesis and surface reconstruction. It achieves an acceleration of over 30 \times in reconstruction and improves visual quality (SSIM) from 0.3755 to 0.7624 compared to traditional SfM with 3D-GS.

1. Introduction

3D reconstruction from a limited number of images has been a long-standing goal in computer vision. Conventional methods for 3D reconstruction, such as 3D Gaussian Splatting (3D-GS)[20], require preprocessing using Structure-from-Motion (SfM) to acquire camera poses and perform Adaptive Density Control (ADC), a heuristic strategy that

densifies sparse SfM point clouds into densely populated 3D primitives. However, SfM processes require densely captured multi-view images with large overlapping regions for feature matching[32] and can be fragile with sparse-view data. Moreover, errors derived from SfM and the distribution of SfM points can significantly degrade 3D-GS optimization, posing challenges to the subsequent ADC process for densification. As shown in Tab. 1, slight perturbations of the initial camera parameters or the point cloud distribution markedly affect reconstruction quality. Many significant efforts have been made to alleviate these strict camera view number requirements by either assuming access to ground-truth camera parameters in sparse-view reconstruction [16, 30, 38, 47], or by relying on a complex ADC strategy [55] to carefully initialize new scene points.

In our work, we tackle sparse-view neural reconstruction from a new perspective. Instead of relying on fragile SfM camera poses and time-consuming sparse-to-dense optimization, we exploit the generalization capabilities of a pre-trained geometry model to initialize pixel-aligned points with reasonable camera pose estimates. Specifically, we present *InstantSplat*, an end-to-end optimization framework to connect 2D images and 3D representations after initialization. This system offers two distinct advantages: (1) it generalizes well to various scene types with minimal multi-view coverage (as few as 2 or 3 images) based on dense initialization and 3D-2D alignment, and (2) it is lightning-fast owing to points redundancy elimination and its end-to-end confidence-aware optimization paradigm using gradient-based photometric error.

InstantSplat incorporates geometric priors from MAS3R [22] to obtain densely covered, pixel-aligned points. To avoid redundancy arising from overlapping regions, we design a co-visibility-based geometry initialization that gradually adds new points through cross-view projection to cover uncovered spaces. Finally, we apply a confidence-aware optimization in which we adjust the learning rate based on the confidence score from the initial geometry. We validate InstantSplat on multiple point-based representations, including 3D Gaussian Splatting [20], 2D surfel-based Gaussian splatting [15], and Mip-Splatting [51], which dramatically reduce its optimization time. Evaluations on the Tanks and Temples [21] and MVImgNet [50] datasets demonstrate that reconstruction can be completed in just 7.5 seconds while significantly improving SSIM from 0.3755 to 0.7624 in a 3-view setting, and further enhancing pose accuracy.

In summary, our main contributions are:

- We address sparse-view neural 3D reconstruction with geometric initialization and rapid photometric adaptation, overcoming the limitations of traditional, fragile SfM methods and the complexities associated with 3D-GS ADC strategies.

	SSIM \uparrow	LPIPS \downarrow
COLMAP+3DGS [20]	0.7633	0.2122
+ Mask 30% SfM Points	0.7406 _(-0.0227)	0.2427 _(+0.0305)
$\pm 1^\circ$ Noise on Rotation	0.3529 _(-0.4104)	0.5265 _(+0.3143)

Table 1. **Sensitivity Analysis in Adaptive Density Control (ADC).** The 3D-GS [20] utilizes camera parameters and sparse points from Structure-from-Motion (SfM). Simply adjusting the point distribution through 30% downsampling poses challenges (LPIPS: 0.2122 \mapsto 0.2427), and slight rotational perturbations in SfM poses lead to substantial performance drops (LPIPS: 0.2122 \mapsto 0.5265). Experiments conducted on the “Bicycle” scene from the MipNeRF360 [2] dataset.

- We introduce a Co-visible Global Geometry Initialization, a technique that effectively avoids redundant points based on inter-frame co-visibility projection, as well as an adaptive optimization where we adjust the learning rate based on initial confidence.
- Our proposed solution is compatible with multiple neural 3D representations, and substantially accelerates scene reconstruction to just a few seconds under sparse-view conditions while simultaneously improving visual quality and pose accuracy.

2. Related Works

3D Representations Novel view synthesis aims to generate unseen views of an object or scene from a given set of images [1, 28]. Neural Radiance Fields (NeRF) [29], enables photo-realistic rendering quality, employs MLPs to represent 3D scenes, taking the directions and positions of 3D points as input and employing volume rendering for image synthesis. Despite its popularity, NeRF faces challenges in terms of speed during both training and inference phases. Subsequent enhancements primarily focus on either enhancing quality [2–4] or improving efficiency [31, 34–36], with few achieving both. Recent advancements in unstructured radiance fields [8, 20, 46] introduce a set of primitives to represent scenes. Notably, 3D Gaussian Splatting (3D-GS) [20] uses anisotropic 3D Gaussians [57] to depict radiance fields, coupled with differentiable splatting for rendering. This method has shown considerable success in rapidly reconstructing complex real-world scenes with high quality. And many works extend 3D-GS for surface reconstruction [15, 52, 53], neural gaussians [26], multi-resolution modeling [11, 51] and feed-forward reconstruction [6, 7, 10, 13, 19, 23, 45, 48, 56]. However, these point-based representations involves a large number of hyperparameters for different datasets, especially for the adaptive density control, which servers as the core function to densify from sparse SfM point cloud to densely covered 3D Gaussian points. However, the optimization of SfM is independent with the followed 3D Gaussian optimization, and the accumulated error cannot be mitigated with current

pipelines. This motivate us to design a holistic, efficient and robust framework to represent the 3D world.

Unconstraint Novel View Synthesis NeRFs and 3DGS require carefully captured hundreds of images to ensure sufficient scene coverage as input and utilize pre-processing Structure-from-Motion (SfM) software, such as COLMAP [32], to compute camera parameters, and sparse SfM point cloud as additional inputs. However, the densely captured images with the strong reliance on COLMAP significantly limits practical applications, it requires the users with expertise in the field of photography and requires significant computing resources (hours for each individual scene). The accumulated error from SfM will propagate to the following differential 3D representation and SfM may fail with captured images without sufficient overlappings and rich textures. To address the challenge of the requisite number of views, various studies have introduced different regularization techniques to optimize the radiance fields. For instance, RegNeRF [30] and SparseNeRF [38] introduces a depth prior loss for geometric regularization. DietNeRF [16], SinNeRF [44], and ReconFusion [42] leverages supervision in the CLIP/DINO-ViT/Diffusion Model to constrain the rendering of unseen views. PixelNeRF [49] and FreeNeRF [47] utilize pre-training and frequency annealing for few-shot NeRF. FSGS [55], and SparseGS [43] employ monocular depth estimators or diffusion models on Gaussian Splatting for sparse-view conditions. However, these methods require known ground-truth camera poses, because SfM algorithms often fail to predict camera poses and point cloud with sparse inputs due to insufficient image correspondences. Therefore, another line of research focuses on COLMAP-free 3D optimization with uncalibrated images as direct input. NeRFmm [41] simultaneously optimizes camera intrinsics, extrinsics, and NeRF training. BARF [24] introduces a coarse-to-fine strategy for encoding camera poses and joint NeRF optimization. SCNeRF [17] adds camera distortion parameterization and employs geometric loss for ray regularization. Similarly, GARF [17] demonstrates that Gaussian-MLPs facilitate more straightforward and accurate joint optimization of pose and scene. SPARF [37] adds Gaussian noise to simulate noisy camera poses. Recent works, such as Nope-NeRF [5], Lu-NeRF [9], LocalRF [27] and CF-3DGS [12], leverage depth information to constrain NeRF or 3DGS optimization. The work in [18] utilizes monocular depth estimator and additional image matching network try to reduce the view number, with roughly hours of optimization for a single scene. These COLMAP-free works generally presume the input are dense video sequences [5, 12] with known viewing order and camera intrinsics [5, 12, 18], and the optimization for each scene (usually several hours) is even longer than COLMAP with NeRF or 3D-GS variants.

In contrast, InstantSplat proposes a different paradigm

that reconstructs using geometric priors while incorporating Gaussian Splatting to jointly optimize camera poses and the 3D model at lightning-fast speed.

3. Method

Overview InstantSplat initializes geometry and poses from the pre-trained MAST3R, converts them into 3D Gaussians, and then jointly optimizes them using an end-to-end framework. First, MAST3R initializes pair-wise geometry, which can be registered into a global coordinate system (Sec.3.1). Next, we perform co-visible redundancy reduction to avoid repeated initialization of 3D primitives, and jointly optimize camera poses and 3D scenes using Gaussian-based Bundle Adjustment (Sec.3.2). The gradient-based joint optimization framework relies on photometric error to align 3D Gaussians with 2D images, employing a confidence-aware optimizer with few optimization steps (Sec. 3.3).

3.1. Preliminary

3D Gaussian Splatting (3D-GS) [20] is an explicit 3D scene representation utilizing a set of 3D Gaussians to model the scene. A 3D Gaussian is parameterized by a mean vector $\mathbf{x} \in \mathbb{R}^3$, an opacity $\alpha \in \mathbb{R}$ and a covariance matrix $\Sigma \in \mathbb{R}^{3 \times 3}$:

$$G(\mathbf{p}, \alpha, \Sigma) = \alpha \exp \left(-\frac{1}{2} (\mathbf{p} - \mathbf{x})^T \Sigma^{-1} (\mathbf{p} - \mathbf{x}) \right) \quad (1)$$

To represent the view-direction-dependent, spherical harmonic (SH) coefficients are attached to each Gaussian, and the color is rendered via $\mathbf{c} = \sum_{i=1}^n \mathbf{c}_i \alpha_i \prod_{j=1}^{i-1} (1 - \alpha_j)$. Here, \mathbf{c}_i , α_i represents the view-dependent color and opacity, calculated from a 2D Gaussian with covariance Σ multiplied by an optimizable per-3D Gaussian's opacity. In summary, 3D-GS uses a set of 3D Gaussians $\{\mathbf{G}_i | i = 1, 2, \dots, n\}$ to represent a scene, where each 3D Gaussian \mathbf{G}_i is characterized by: position $\mathbf{x} \in \mathbb{R}^3$, color defined by spherical harmonics coefficients $\text{SH} \in \mathbb{R}^{(k+1)^2 \times 3}$ (where k represents the degrees of freedom), opacity $\alpha \in \mathbb{R}$, rotation $\mathbf{q} \in \mathbb{R}^4$ and scaling $\mathbf{s} \in \mathbb{R}^3$.

Distinguished from 3D-GS, 2D-GS [14] proposes that reducing one scaling dimension to zero and approximating the primitive as a surface can improve view consistency. To implement this, 2D-GS replaces the volumetric representations used in 3D-GS with planar disks, which are defined within the local tangent plane and mathematically expressed as follows:

$$G(\mathbf{p}) = \exp \left(-\frac{u(\mathbf{p})^2 + v(\mathbf{p})^2}{2} \right) \quad (2)$$

where $u(\mathbf{p})$ and $v(\mathbf{p})$ are local UV space coordinates.

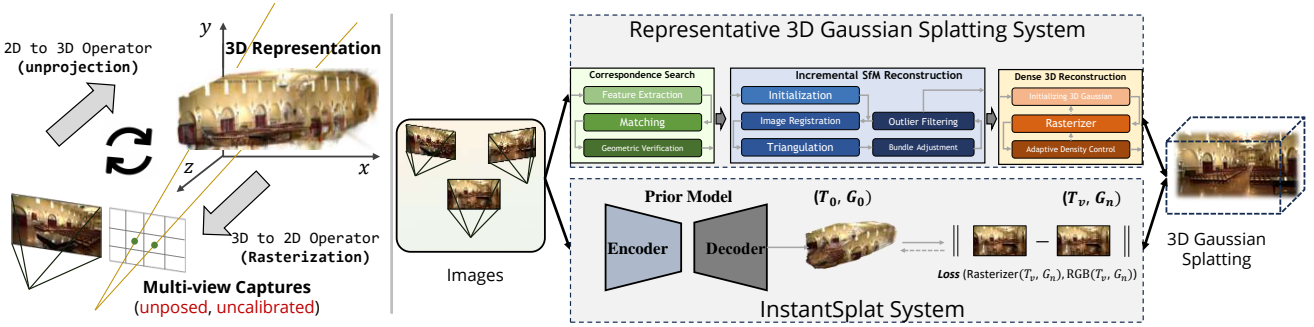


Figure 2. Overall Framework. **InstantSplat** synergizes the geometry priors from the pre-trained MAST3R model and utilizes Gaussian Splatting to jointly optimize camera parameters and the 3D scenes.

During the rendering process, 2D-GS substitutes direct affine transformations with three non-parallel planes to define ray-splat intersections. Following this, rasterization is applied after a low-pass filter to produce smoother results.

MASt3R is a feed-forward Multi-View Stereo model where it regresses the pixel-aligned point maps directly from raw images. It utilizes a Transformer architecture with cross-view information flow to predict the $\hat{\mathbf{P}}_{1,1}$ and $\hat{\mathbf{P}}_{2,1}$, obtained from two corresponding views $\{1, 2\}$ where the camera origin is view 1, on which the ground-truth is defined. The regression loss for training MASt3R is as:

$$\mathcal{L}_{\text{reg}} = \left\| \frac{1}{z_i} \cdot \mathbf{P}_{v,1} - \frac{1}{\hat{z}_i} \cdot \hat{\mathbf{P}}_{v,1} \right\| \quad (3)$$

The view $v \in \{1, 2\}$, \mathbf{P} and $\hat{\mathbf{P}}$ are the predicted and ground-truth point maps, respectively. Normalizing factors z_i , \hat{z}_i are introduced to make the reconstruction invariant to scale. These are simply defined as the mean distance of all valid 3D points to the origin. It also regresses the pixel-aligned confidence score $\mathbf{O}_{v,1}^i$ and optimizes as:

$$\mathcal{L}_{\text{conf}} = \sum_{v \in \{1, 2\}} \sum_{i \in \mathbf{D}^v} \mathbf{O}_{v,1}^i \cdot \mathcal{L}_{\text{reg}}(v, i) - \alpha \cdot \log \mathbf{O}_{v,1}^i, \quad (4)$$

where α is a hyper-parameter controlling the regularization, encouraging the network to extrapolate in harder areas.

3.2. Co-visible Global Geometry Initialization

Scaling Pairwise to Global Alignment With the off-the-shelf stereo model, MASt3R, we regress a set of stereo point maps along with calculated camera intrinsics and extrinsics following Sec. 3.1. To align these pair wise predictions into a globally aligned results, we follow MASt3R to build a complete connectivity graph $\mathcal{G}(\mathcal{V}, \mathcal{E})$ of all the N input views, where the vertices \mathcal{V} and each edge $e = (I_i, I_j) \in \mathcal{E}$ indicate a shared visual content between images I_i and I_j ($i, j \in \{1, 2, \dots, N\}, i \neq j$). To convert the initially predicted point map $\{(\mathbf{P}_i \in \mathbb{R}^{H \times W \times 3})\}_{i=1}^N$ to be a globally aligned one $\{(\hat{\mathbf{P}}_i \in \mathbb{R}^{H \times W \times 3})\}_{i=1}^N$, we follow the

MASt3R to update these point maps, transformation matrix, and a scale factor into globally coordinate system. Please refer to the supplementary material for detailed description. However, the pairwise predicted focal lengths remain inconsistent post-optimization. Assuming a single-camera setup akin to COLMAP for capturing a scene, we stabilize the estimated focal lengths by averaging them across all training views: $\bar{f} = \frac{1}{N} \sum_{i=1}^N f_i^*$ which is simple but significantly improve optimized visual quality.

Co-visible Redundancy Elimination Utilizing point maps from all training images typically results in redundancy, manifested through overlapping regions that produce duplicated, pixel-aligned point clouds. This not only increases the free parameters in scene representation but also slows down the optimization process. To combat this, we exploit co-visibility across training images to eliminate these duplicate pixels. **View ranking** is conducted by computing the average confidence levels from the confidence maps of each image, with a higher average indicating a more accurate initial geometry from the 3D prior model. We prune points from views with lower confidence scores to enhance point quality, measured by the view confidence score,

$$s_i = \frac{1}{|\mathbf{O}_i|} \sum_{o \in \mathbf{O}_i} o \quad (5)$$

where s_i denotes the average confidence score of view i .

Co-visible redundancy elimination starts with the view (j) having the lowest average confidence score, where we combine point maps from views with higher average confidence score than view j , $\{(\hat{\mathbf{P}}_i \in \mathbb{R}^{H \times W \times 3})\}_{i=1, i \neq j, s_i > s_j}^N$, and project them onto view j . Depth ambiguity is addressed through a depth verification process, pruning points only if the difference between the projected and original depth values is higher than a predefined threshold: $\Delta d = |d_{\text{proj}} - d_{\text{orig}}|$, where d_{orig} are obtained from MASt3R. This procedure is iterated in ascending order across all images, ultimately generating binary masks $\{(\mathcal{M}_i \in \mathbb{R}^{H \times W \times 1})\}_{i=1}^N$ to filter out redundant points. More formally, the cross-view

co-visibility check for removing redundancy in view j can be written as:

$$\mathbf{D}_{\text{proj},j} = \bigcap_{\{i|s_i > s_j\}} \text{Proj}_j(\tilde{\mathbf{P}}_i) \quad (6)$$

$$\mathcal{M}_j = \begin{cases} 1 & \text{if } |\mathbf{D}_{\text{proj},j} - \mathbf{D}_{\text{orig},j}| < \theta \\ 0 & \text{otherwise} \end{cases} \quad (7)$$

$$\tilde{\mathbf{P}}_j = (1 - \mathcal{M}_j) \cdot \tilde{\mathbf{P}}_j \quad (8)$$

where Proj is the function applying the projection operator across all views except view i ($v_i \geq v_j$). \mathcal{M}_j is the visibility mask, determined by comparing the projected depth $d_{\text{proj},j}$ to the original depth $d_{\text{orig},j}$. Points with depth differences below a threshold θ are considered visible and consistent, thus redundant. We use inverse of \mathcal{M}_j to mask out redundant points.

3.3. Rapid Optimization

Confidence-aware Optimizer In our pursuit to refine the accuracy of scene reconstruction, we introduce a confidence-aware per-point optimizer designed to facilitate convergence during self-supervised optimization. This approach is tailored to dynamically adjust learning rates based on the per-point confidence as detailed in Sec. 3.2. By prioritizing points with lower confidence, which are more susceptible to errors, we ensure a targeted and efficient optimization process. The calibration of confidence scores involves normalizing them into a proper range, thereby addressing points in need of significant corrections. The normalization and adjustment process is mathematically outlined as follows: $\mathbf{O}_{\text{norm}} = (1 - \text{sigmoid}(\mathbf{O}_{\text{init}})) \cdot \beta$ where β is a hyperparameter used to fine-tune the scaling effect, optimizing the learning rates to enhance the convergence.

Joint Optimization for Alignment Given multiple views and a 3D representation with initialized poses, represented by a set of Gaussians \mathbf{G} , and camera poses \mathbf{T} , we employ the pre-built rasterizer from Gaussian Splatting as a differentiable operator to render the images corresponding to the target poses \mathbf{T} . Gradient descent with photometric error minimization is used to reduce the discrepancy between the optimizable 3D representation and 2D observations, iteratively refining \mathbf{G} , and \mathbf{T} toward representative orientations:

$$\mathbf{G}^*, \mathbf{T}^* = \arg \min_{\mathbf{G}, \mathbf{T}} \sum_{v \in N} \sum_{i=1}^{HW} \left\| \tilde{\mathbf{C}}_v^i - \mathbf{C}_v^i(\mathbf{G}, \mathbf{T}) \right\|$$

The \mathbf{C} denotes the rasterization function applied to \mathbf{G} at \mathbf{T} , while $\tilde{\mathbf{C}}$ represents the observed 2D images.

Aligning Camera Poses on Test Views Unlike benchmark datasets where camera pose estimation and calibration are pre-computed with access to all training and testing

views, a COLMAP-free setting requires additional steps to regress the poses for the test views. Similar to INeRF [41], we freeze the 3D model learned by training images, while optimizing the camera poses for the test views. This optimization process focuses on minimizing the photometric discrepancies between the synthesized images and the actual images on test views, aiming to achieve alignment between the 3D model and test images for evaluating visual quality and pose estimation metrics.

4. Experiments

4.1. Experimental Setup

Datasets. Following methodologies from previous research [5, 12], we evaluated our InstantSplat on eight scenes from the **Tanks and Temples** dataset [21] with view counts ranging from 3 to 12. Additionally, we tested on seven outdoor scenes from the **MVImgNet** dataset [50], covering diverse scene types including Car, Suv, Bicycle, Chair, Ladder, Bench, and Table. Our experiments also extend to in-the-wild data, incorporating frames from the **Sora** video ([link](#)), and navigation stereo camera data from the **Perseverance Rover (NASA)**, along with three randomly sampled training views from the DL3DV-10K dataset [25].

Train/Test Datasets Split. For both training and evaluation, 12 images from each dataset were sampled, spanning the entire set. The test set includes 12 images uniformly chosen to exclude the first and last frames, while the training set comprises an equal number of images selected from the remainder, ensuring sparse-view training setting. This uniform sampling approach was applied consistently across both MVImgNet and Tanks and Temples datasets.

Metrics. We evaluate our approach on benchmark datasets [21, 50] across three tasks: novel view synthesis, camera pose estimation, and depth estimation. For novel view synthesis, we use Peak Signal-to-Noise Ratio (PSNR), Structural Similarity Index Measure (SSIM) [40], and Learned Perceptual Image Patch Similarity (LPIPS) [54]. For camera pose estimation, we report the Absolute Trajectory Error (ATE) as defined in [5], using COLMAP poses from all dense views as ground-truth references. For depth estimation, we evaluate using the Absolute Relative Error (Rel) and the Inlier Ratio (τ) with a threshold of 1.03, following DUST3R [39].

Baselines. Our comparisons on COLMAP-free methods include Nope-NeRF [5] and CF-3DGGS [12], both supported by monocular depth maps and ground-truth camera intrinsics. We also consider NeRFmm [41], which involves joint optimization of NeRF and all camera parameters. Additionally, we compare our method with 3D-GS [20] and

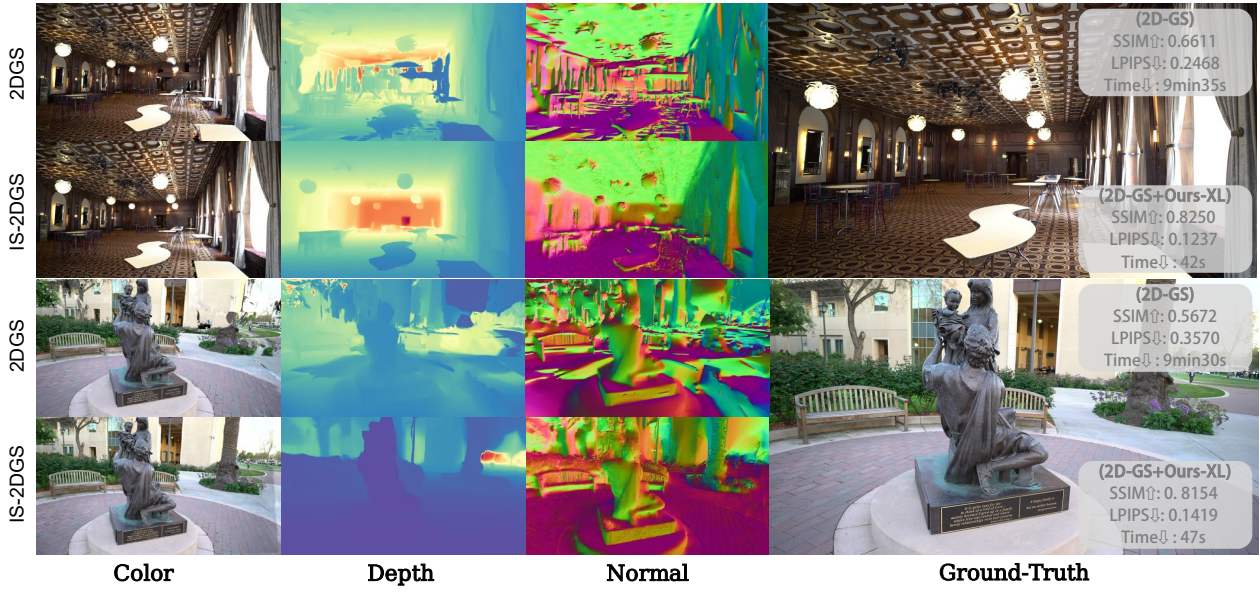


Figure 3. **Visual Comparisons between 2D-GS and InstantSplat-2D-GS under 3-view setting.** We present the rendering results of RGB images, depth maps, and normal maps from the Tanks and Temples dataset. The corresponding SSIM, LPIPS, and training time metrics are displayed on the right. Here, IS is used as an abbreviation for InstantSplat.

Table 2. **Quantitative Evaluations on Tanks and Temples Datasets.** Our method achieves significantly clearer details (lower LPIPS) compared to other COLMAP-free methods, even with an optimization time of only ~ 7.5 seconds (**Ours-S**), and avoids artifacts caused by noisy pose estimation, as quantified by Absolute Trajectory Error (ATE). Extending training time further improves rendering quality. InstantSplat also demonstrates superior camera pose estimation accuracy in ATE with ground truth scale. The optimization iterations is set 200 for **Ours-S**, and 1,000 for **Ours-XL**.

	Training Time			SSIM			LPIPS			ATE		
	3-view	6-view	12-view	3-view	6-view	12-view	3-view	6-view	12-view	3-view	6-view	12-view
COLMAP + 3DGS [20]	4min28s	6min44s	8min11s	0.3755	0.5917	0.7163	0.5130	0.3433	0.2505	-	-	-
COLMAP + FSGS [55]	2min37s	3min16s	3min49s	0.5701	0.7752	0.8479	0.3465	0.1927	0.1477	-	-	-
NoPe-NeRF [5]	33min	47min	84min	0.4570	0.5067	0.6096	0.6168	0.5780	0.5067	0.2828	0.1431	0.1029
CF-3DGS [12]	1min6s	2min14s	3min30s	0.4066	0.4690	0.5077	0.4520	0.4219	0.4189	0.1937	0.1572	0.1031
NeRF-mm [41]	7min42s	14min40s	29min42s	0.4019	0.4308	0.4677	0.6421	0.6252	0.6020	0.2721	0.2329	0.1529
Ours-S	7.5s	13.0s	32.6s	0.7624	0.8300	0.8413	0.1844	0.1579	0.1654	0.0191	0.0172	0.0110
Ours-XL	25.4s	29.0s	44.3s	0.7615	0.8453	0.8785	0.1634	0.1173	0.1068	0.0189	0.0164	0.0101

FSGS [55], which utilize COLMAP for pre-computing the camera parameters.

Implementation Details. Our implementation is built using the PyTorch framework. Optimization iterations are set to 200 for **Ours-S** and 1,000 for **Ours-XL**, striking a balance between quality and training efficiency. During evaluation, 500 iterations are used for test view optimization. The parameter β is fixed at 100. For multi-view stereo (MVS) depth map prediction, MAST3R is configured with a resolution of 512 and the `cupy` library is used to accelerate the initialization. All experiments are conducted on a single Nvidia A100 GPU to ensure fair comparisons.

4.2. Experimental Results

Quantitative and Qualitative Results on Novel-view Synthesis We evaluate novel-view synthesis and pose estimation on the Tanks and Temples dataset, with results summarized in Tab.2 and Fig.4.

Nope-NeRF [5], which leverages Multilayer Perceptrons (MLPs), delivers promising pose estimation accuracy with dense video sequences. However, it often generates overly blurred images (see the third column in Fig. 4), primarily due to the heavy constraints imposed by its geometric field. Additionally, it suffers from prolonged training times for a single scene and inference delays (~ 3 seconds per frame for rendering one image). CF-3DGS [12], which em-

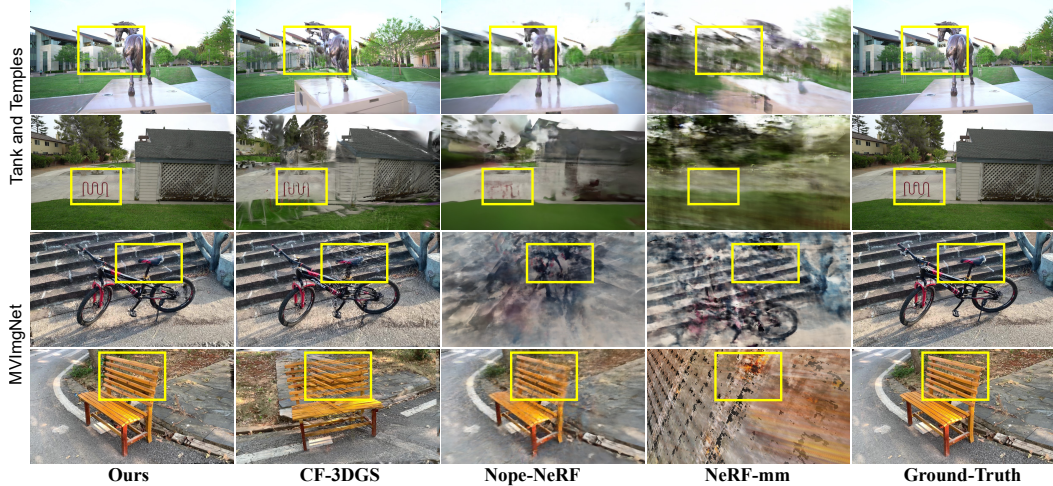


Figure 4. **Visual Comparisons** between InstantSplat and various COLMAP-free methods. InstantSplat achieves faithful 3D reconstruction and renders novel views with as few as three training images on the Tanks and Temples datasets, and the MVImgNet datasets.

Table 3. **Quantitative Evaluations on MVImgNet Datasets.** Our method renders significantly clearer details (by LPIPS) compared to other methods, devoid of artifacts typically associated with noisy pose estimation (e.g., CF-3DGS [12], NeRFmm [41] and NoPe-NeRF [5]). COLMAP on full views as the ground-truth reference. Our method produces more accurate camera pose estimation in the Absolute Trajectory Error (ATE) than previous COLMAP-free methods, quantified using the ground truth scale.

	Training Time			SSIM			LPIPS			ATE		
	3-view	6-view	12-view	3-view	6-view	12-view	3-view	6-view	12-view	3-view	6-view	12-view
NoPe-NeRF [5]	37min42s	53min	95min	0.4326	0.4329	0.4686	0.6168	0.6614	0.6257	0.2780	0.1740	0.1493
CF-3DGS [12]	3min47s	7min29s	10min36s	0.3414	0.3544	0.3655	0.4520	0.4326	0.4492	0.1593	0.1981	0.1243
NeRF-mm [41]	8min35s	16min30s	33min14s	0.3752	0.3685	0.3718	0.6421	0.6252	0.6020	0.2721	0.2376	0.1529
Ours	10.4s	15.4s	34.1s	0.5489	0.6835	0.7050	0.3941	0.2980	0.3033	0.0184	0.0259	0.0165
Our-XL	35.7s	48.1s	76.7s	0.5628	0.6933	0.7321	0.3688	0.2611	0.2421	0.0184	0.0259	0.0164

Table 4. **Ablation Study** for validating design choices. We opt for the **XL** setting, where 1,000 iterations are adopted to ensure reconstruction quality.

Model	Train \downarrow	FPS \uparrow	SSIM \uparrow	LPIPS \downarrow	ATE \downarrow
Baseline by Stitching	51s	150	0.8014	0.1654	0.0142
+ Focal Averaging	51s	150	0.8406	0.1288	0.0115
+ Co-visibility Geometry Init.	45s	181	0.8411	0.1313	0.0115
+ Confidence-aware Optimizer	45s	181	0.8553	0.1277	0.0115
+ Joint Optimization	45s	181	0.8822	0.1050	0.0102

loys Gaussian Splatting with local and global optimization stages along with adaptive density control and opacity reset policies, encounters artifacts when rendering from novel viewpoints. These artifacts result from its complex optimization pipeline and erroneous pose estimations, as shown in the second column of Fig. 4. Moreover, both Nope-NeRF and CF-3DGS assume accurate focal lengths, limiting their robustness in scenarios with focal length uncertainties. NeRFmm, designed for simultaneous optimization of camera parameters and the radiance field, often struggles with suboptimal results due to the inherent challenges of naive joint optimization.

Pose metrics, as reflected in Tab. 2, reveal significant artifacts caused by sparse observations and inaccurately esti-

mated poses. These limitations are particularly pronounced in CF-3DGS and Nope-NeRF, which depend on dense video sequences, akin to SLAM, and encounter difficulties when these dense frames are downsampled to sparse multi-view images. In contrast, our method initializes with the MVS scene structure and employs a gradient-based joint optimization framework, providing enhanced robustness and superior performance.

We demonstrate the geometric accuracy of InstantSplat by integrating it with 2D Gaussian Splatting, visualizing rasterized depth and normal maps. As shown in Fig. 3 and Tab. 6, under the 3-view setting, InstantSplat significantly improves geometry quality, benefiting from dense initialization and the joint optimization framework. Additionally, we validate InstantSplat within the multi-resolution Mip-Splatting framework. Tab. 7 shows evaluations on the Tanks and Temples dataset using the original resolution for testing while varying the training resolution. InstantSplat consistently enhances sparse-view rendering metrics.

Further experiments on the MVImgNet dataset with 3, 6, and 12 training images are presented in Tab. 3. This section demonstrates that InstantSplat consistently outperforms all baselines across all evaluated datasets and metrics. Please refer to our supplementary video for additional visu-

alizations, including in-the-wild test cases such as the Sora video, DL3DV-10K dataset, and stereo image pairs from the Mars rover.

4.3. Ablations and Analysis

We conducted ablation studies to validate our design choices, transitioning from the use of non-differentiable Structure-from-Motion (SfM) complemented by Gaussian Splatting with adaptive density control, to adopting Multi-View Stereo (MVS) with Co-visible Global Geometry Initialization, Confidence-aware Optimizer and Joint Optimization for efficient and robust sparse-view 3D modeling. Experiments were conducted using 12 training views on all scenes in the Tanks and Temples dataset, with COLMAP poses derived from full dense views serving as ground truth, unless otherwise specified.

- Question 1: How does the quality of multi-view stereo predictions impact performance?
- Question 2: What is the impact of focal averaging on the results?
- Question 3: Does co-visible geometric initialization effectively reduce redundancy and preserve reconstruction accuracy?
- Question 4: Is Joint Optimization essential for accurate rendering?
- Question 5: Can InstantSplat achieve rendering quality comparable to methods using dense-view images, but with sparse-view inputs?

For **Q1**, the evaluation of camera pose accuracy from MAS3R reveals considerable differences in rendering quality and pose accuracy, as shown in the first row of Tab. 4. This baseline is implemented by directly stitching together MAS3R’s point cloud and camera parameters for the initialization of 3D-GS to optimize the Gaussian attributes. For **Q2**, aggregating focal lengths from all images stabilizes the 3D representation optimization, evidenced by results in the second row.

For **Q3**, co-visible geometry initialization significantly enhances FPS by minimizing redundancy while preserving robust rendering accuracy, as elaborated in the third row.

For **Q4**, Joint Optimization, through self-supervised optimization, substantially improves visual and pose metrics by aligning the 3D and 2D representations.

For **Q5**, InstantSplat using 12 training images approaches the rendering quality of denser-view methods as measured by the Learned Perceptual Image Patch Similarity (LPIPS), indicative of near-human perceptual sharpness. However, it exhibits discrepancies in pose estimation accuracy (ATE), inevitably leading to lower PSNR metrics (Tab. 5).

5. Conclusion

We present InstantSplat, the first system that synergizes the geometric priors from pre-trained deep models, while per-

Table 5. Performance comparison between InstantSplat (ours) with 12 training views, CF-3DGS and 3D-GS with dense (100-400) training views on the Tanks and Temples dataset. We report the LPIPS, reconstruction time, and pose accuracy.

	Views ↓	Time ↓	LPIPS ↓	ATE ↓
CF-3DGS [12]	100-400	~30min	0.09	0.004
COLMAP+3DGS [20]	100-400	~30min	0.10	-
InstantSplat (Ours)	12	~45s	0.10	0.010

Table 6. **InstantSplat with 2D-GS.** InstantSplat demonstrates strong compatibility with 2D-GS, notably improving sparse-view rendering quality and depth accuracy while also accelerating scene reconstruction. We opt for 1,500 optimization iterations to balance reconstruction quality and efficiency.

	View Num.	Train Time	Novel View Synthesis			Depth Estimation	
			PSNR↑	SSIM↑	LPIPS↓	rel↓	↑
2D-GS +InstantSplat	3	45s	21.90	0.7447	0.1920	28.7557	26.1918
	6	58s	24.99	0.8281	0.1450	29.9461	25.7376
	12	98s	26.07	0.8557	0.1407	29.4234	25.3569
2D-GS	3	10min3s	15.09	0.5495	0.3719	59.8629	5.2962
	6	11min22s	19.88	0.7251	0.2388	45.4608	17.8145
	12	11min54s	23.70	0.8184	0.1723	40.1948	20.1998

Table 7. **InstantSplat with Mip-Splatting.** Both methods were trained in sparse view settings, with variations in training and evaluation resolutions consistent with Mip-Splatting protocols. InstantSplat demonstrates compatibility with Mip-Splatting, significantly enhancing sparse-view rendering quality.

	Training Resolution	3-view		12-view	
		SSIM	LPIPS	SSIM	LPIPS
Mip-Splatting + Ours-XL	1	0.7647	0.1618	0.8415	0.1305
	1/2 Res.	0.7456	0.2343	0.7945	0.2027
	1/4 Res.	0.6630	0.3774	0.7204	0.3348
Mip-Splatting	1	0.5422	0.3780	0.7947	0.1901
	1/2 Res.	0.5777	0.3939	0.7703	0.2418
	1/4 Res.	0.5477	0.4840	0.6664	0.3770

forming joint optimization for accurate 3D scene reconstruction and camera pose estimation. InstantSplat is efficient and effective under sparse-view reconstruction, capable of building a 3D model in just a few seconds, thereby demonstrating superior practicality in real-world scenarios. It aligns the 3D representation and 2D images with a differentiable operator and avoids the time-consuming and fragile Structure-from-Motion and Adaptive Density Control. InstantSplat also introduces co-visibility-based initialization as well as confidence-aware optimization to enhance robustness. Compared with previous best-performing COLMAP-free methods [5, 12], InstantSplat dramatically reduces the required number of views from hundreds to just a few and demonstrates robustness across in-the-wild datasets, as well as adaptability to many point-based representations.

However, InstantSplat faces limitations when applied to scenes with more than a few hundred images due to the pixel-aligned initialization. Addressing this issue through progressive alignment with Gaussian pruning techniques will be the focus of future research.

References

[1] Shai Avidan and Amnon Shashua. Novel view synthesis in tensor space. In *Proceedings of IEEE Computer Society Conference on Computer Vision and Pattern Recognition*, pages 1034–1040. IEEE, 1997. [2](#)

[2] Jonathan T. Barron, Ben Mildenhall, Dor Verbin, Pratul P. Srinivasan, and Peter Hedman. Mip-NeRF 360: Unbounded Anti-Aliased Neural Radiance Fields. *2022 IEEE/CVF Conference on Computer Vision and Pattern Recognition (CVPR)*, pages 5460–5469, 2022. [2](#)

[3] Jonathan T Barron, Ben Mildenhall, Dor Verbin, Pratul P Srinivasan, and Peter Hedman. Mip-nerf 360: Unbounded anti-aliased neural radiance fields. In *Proceedings of the IEEE/CVF Conference on Computer Vision and Pattern Recognition*, pages 5470–5479, 2022.

[4] Jonathan T Barron, Ben Mildenhall, Dor Verbin, Pratul P Srinivasan, and Peter Hedman. Zip-nerf: Anti-aliased grid-based neural radiance fields. In *Proceedings of the IEEE/CVF International Conference on Computer Vision*, pages 19697–19705, 2023. [2](#)

[5] Wenjing Bian, Zirui Wang, Kejie Li, Jia-Wang Bian, and Victor Adrian Prisacariu. Nope-nerf: Optimising neural radiance field with no pose prior. In *Proceedings of the IEEE/CVF Conference on Computer Vision and Pattern Recognition*, pages 4160–4169, 2023. [3, 5, 6, 7, 8, A12](#)

[6] David Charatan, Sizhe Lester Li, Andrea Tagliasacchi, and Vincent Sitzmann. pixelsplat: 3d gaussian splats from image pairs for scalable generalizable 3d reconstruction. In *Proceedings of the IEEE/CVF Conference on Computer Vision and Pattern Recognition*, pages 19457–19467, 2024. [2](#)

[7] Yuedong Chen, Haofei Xu, Chuanxia Zheng, Bohan Zhuang, Marc Pollefeys, Andreas Geiger, Tat-Jen Cham, and Jianfei Cai. Mvsplat: Efficient 3d gaussian splatting from sparse multi-view images. In *European Conference on Computer Vision*, pages 370–386. Springer, 2025. [2](#)

[8] Zhang Chen, Zhong Li, Liangchen Song, Lele Chen, Jingyi Yu, Junsong Yuan, and Yi Xu. Neurbf: A neural fields representation with adaptive radial basis functions. In *Proceedings of the IEEE/CVF International Conference on Computer Vision*, pages 4182–4194, 2023. [2](#)

[9] Zezhou Cheng, Carlos Esteves, Varun Jampani, Abhishek Kar, Subhransu Maji, and Ameesh Makadia. Lu-nerf: Scene and pose estimation by synchronizing local unposed nerfs. In *Proceedings of the IEEE/CVF International Conference on Computer Vision*, pages 18312–18321, 2023. [3](#)

[10] Zhiwen Fan, Jian Zhang, Wenyan Cong, Peihao Wang, Renjie Li, Kairun Wen, Shijie Zhou, Achuta Kadambi, Zhangyang Wang, Danfei Xu, et al. Large spatial model: End-to-end unposed images to semantic 3d. *arXiv preprint arXiv:2410.18956*, 2024. [2](#)

[11] Guofeng Feng, Siyan Chen, Rong Fu, Zimu Liao, Yi Wang, Tao Liu, Zhilin Pei, Hengjie Li, Xingcheng Zhang, and Bo Dai. Flashgs: Efficient 3d gaussian splatting for large-scale and high-resolution rendering. *arXiv preprint arXiv:2408.07967*, 2024. [2](#)

[12] Yang Fu, Sifei Liu, Amey Kulkarni, Jan Kautz, Alexei A Efros, and Xiaolong Wang. Colmap-free 3d gaussian splatting. *arXiv preprint arXiv:2312.07504*, 2023. [3, 5, 6, 7, 8, A12](#)

[13] Sunghwan Hong, Jaewoo Jung, Heeseong Shin, Jisang Han, Jiaolong Yang, Chong Luo, and Seungryong Kim. Pf3plat: Pose-free feed-forward 3d gaussian splatting. *arXiv preprint arXiv:2410.22128*, 2024. [2](#)

[14] Binbin Huang, Zehao Yu, Anpei Chen, Andreas Geiger, and Shenghua Gao. 2d gaussian splatting for geometrically accurate radiance fields. In *SIGGRAPH 2024 Conference Papers*. Association for Computing Machinery, 2024. [3](#)

[15] Binbin Huang, Zehao Yu, Anpei Chen, Andreas Geiger, and Shenghua Gao. 2d gaussian splatting for geometrically accurate radiance fields. In *ACM SIGGRAPH 2024 Conference Papers*, pages 1–11, 2024. [2](#)

[16] Ajay Jain, Matthew Tancik, and Pieter Abbeel. Putting nerf on a diet: Semantically consistent few-shot view synthesis. In *Proceedings of the IEEE/CVF International Conference on Computer Vision*, pages 5885–5894, 2021. [2, 3](#)

[17] Yoonwoo Jeong, Seokjun Ahn, Christopher Choy, Anima Anandkumar, Minsu Cho, and Jaesik Park. Self-calibrating neural radiance fields. In *Proceedings of the IEEE/CVF International Conference on Computer Vision*, pages 5846–5854, 2021. [3](#)

[18] Kaiwen Jiang, Yang Fu, Yash Belhe, Xiaolong Wang, Hao Su, Ravi Ramamoorthi, et al. A construct-optimize approach to sparse view synthesis without camera pose. *arXiv preprint arXiv:2405.03659*, 2024. [3](#)

[19] Haian Jin, Hanwen Jiang, Hao Tan, Kai Zhang, Sai Bi, Tianyuan Zhang, Fujun Luan, Noah Snavely, and Zexiang Xu. Lvsm: A large view synthesis model with minimal 3d inductive bias. *arXiv preprint arXiv:2410.17242*, 2024. [2](#)

[20] Bernhard Kerbl, Georgios Kopanas, Thomas Leimkühler, and George Drettakis. 3d gaussian splatting for real-time radiance field rendering. *ACM Transactions on Graphics (ToG)*, 42(4):1–14, 2023. [1, 2, 3, 5, 6, 8, A12](#)

[21] Arno Knapitsch, Jaesik Park, Qian-Yi Zhou, and Vladlen Koltun. Tanks and temples: Benchmarking large-scale scene reconstruction. *ACM Transactions on Graphics (ToG)*, 36(4):1–13, 2017. [2, 5, A12](#)

[22] Vincent Leroy, Yohann Cabon, and Jérôme Revaud. Grounding image matching in 3d with mast3r. *arXiv preprint arXiv:2406.09756*, 2024. [1, 2, A12](#)

[23] Hao Li, Yuanyuan Gao, Chenming Wu, Dingwen Zhang, Yalun Dai, Chen Zhao, Haocheng Feng, Errui Ding, Jingdong Wang, and Junwei Han. Ggrt: Towards pose-free generalizable 3d gaussian splatting in real-time. *CoRR*, 2024. [2](#)

[24] Chen-Hsuan Lin, Wei-Chiu Ma, Antonio Torralba, and Simon Lucey. Barf: Bundle-adjusting neural radiance fields. In *Proceedings of the IEEE/CVF International Conference on Computer Vision*, pages 5741–5751, 2021. [3](#)

[25] Lu Ling, Yichen Sheng, Zhi Tu, Wentian Zhao, Cheng Xin, Kun Wan, Lantao Yu, Qianyu Guo, Zixun Yu, Yawen Lu, et al. Dl3dv-10k: A large-scale scene dataset for deep learning-based 3d vision. In *Proceedings of the IEEE/CVF Conference on Computer Vision and Pattern Recognition*, pages 22160–22169, 2024. [5, A12](#)

[26] Tao Lu, Mulin Yu, Lining Xu, Yuanbo Xiangli, Limin Wang, Dahua Lin, and Bo Dai. Scaffold-gs: Structured 3d gaussians for view-adaptive rendering. In *Proceedings of the IEEE/CVF Conference on Computer Vision and Pattern Recognition*, pages 20654–20664, 2024. 2

[27] Andreas Meuleman, Yu-Lun Liu, Chen Gao, Jia-Bin Huang, Changil Kim, Min H Kim, and Johannes Kopf. Progressively optimized local radiance fields for robust view synthesis. In *Proceedings of the IEEE/CVF Conference on Computer Vision and Pattern Recognition*, pages 16539–16548, 2023. 3

[28] Ben Mildenhall, Pratul P Srinivasan, Rodrigo Ortiz-Cayon, Nima Khademi Kalantari, Ravi Ramamoorthi, Ren Ng, and Abhishek Kar. Local light field fusion: Practical view synthesis with prescriptive sampling guidelines. *ACM Transactions on Graphics (TOG)*, 38(4):1–14, 2019. 2

[29] Ben Mildenhall, Pratul P Srinivasan, Matthew Tancik, Jonathan T Barron, Ravi Ramamoorthi, and Ren Ng. Nerf: Representing Scenes As Neural Radiance Fields for View Synthesis. *Communications of the ACM*, 65(1):99–106, 2021. 2

[30] Michael Niemeyer, Jonathan T Barron, Ben Mildenhall, Mehdi SM Sajjadi, Andreas Geiger, and Noha Radwan. Reg-nerf: Regularizing neural radiance fields for view synthesis from sparse inputs. *arXiv preprint arXiv:2112.00724*, 2021. 2, 3

[31] Eric Penner and Li Zhang. Soft 3D Reconstruction for View Synthesis. *ACM Transactions on Graphics (TOG)*, 36(6):1–11, 2017. 2

[32] Johannes L Schonberger and Jan-Michael Frahm. Structure-from-motion revisited. In *Proceedings of the IEEE conference on computer vision and pattern recognition*, pages 4104–4113, 2016. 2, 3, A12

[33] Philipp Schröppel, Jan Bechtold, Artemij Amiranashvili, and Thomas Brox. A benchmark and a baseline for robust multi-view depth estimation. In *2022 International Conference on 3D Vision (3DV)*, pages 637–645. IEEE, 2022. A12

[34] Steven M Seitz and Charles R Dyer. Photorealistic Scene Reconstruction by Voxel Coloring, 2002. US Patent 6,363,170. 2

[35] Pratul P Srinivasan, Richard Tucker, Jonathan T Barron, Ravi Ramamoorthi, Ren Ng, and Noah Snavely. Pushing the Boundaries of View Extrapolation With Multiplane Images. In *Proceedings of the IEEE/CVF Conference on Computer Vision and Pattern Recognition*, pages 175–184, 2019.

[36] Pratul P Srinivasan, Ben Mildenhall, Matthew Tancik, Jonathan T Barron, Richard Tucker, and Noah Snavely. Lighthouse: Predicting Lighting Volumes for Spatially-Coherent Illumination. In *Proceedings of the IEEE/CVF Conference on Computer Vision and Pattern Recognition*, pages 8080–8089, 2020. 2

[37] Prune Truong, Marie-Julie Rakotosaona, Fabian Manhardt, and Federico Tombari. Sparf: Neural radiance fields from sparse and noisy poses. In *Proceedings of the IEEE/CVF Conference on Computer Vision and Pattern Recognition*, pages 4190–4200, 2023. 3

[38] Guangcong Wang, Zhaoxi Chen, Chen Change Loy, and Ziwei Liu. Sparsenerf: Distilling depth ranking for few-shot novel view synthesis. *arXiv preprint arXiv:2303.16196*, 2023. 2, 3

[39] Shuzhe Wang, Vincent Leroy, Yohann Cabon, Boris Chidlovskii, and Jerome Revaud. Dust3r: Geometric 3d vision made easy. *arXiv preprint arXiv:2312.14132*, 2023. 5, A12

[40] Zhou Wang, Alan C Bovik, Hamid R Sheikh, and Eero P Simoncelli. Image quality assessment: from error visibility to structural similarity. *IEEE transactions on image processing*, 13(4):600–612, 2004. 5

[41] Zirui Wang, Shangzhe Wu, Weidi Xie, Min Chen, and Victor Adrian Prisacariu. Nerf-: Neural radiance fields without known camera parameters. *arXiv preprint arXiv:2102.07064*, 2021. 3, 5, 6, 7, A12

[42] Rundi Wu, Ben Mildenhall, Philipp Henzler, Keunhong Park, Ruiqi Gao, Daniel Watson, Pratul P Srinivasan, Dor Verbin, Jonathan T Barron, Ben Poole, et al. Reconfusion: 3d reconstruction with diffusion priors. *arXiv preprint arXiv:2312.02981*, 2023. 3

[43] Haolin Xiong, Sairisheek Muttukuru, Rishi Upadhyay, Pradyumna Chari, and Achuta Kadambi. Sparsegs: Real-time 360 $\{\backslash\deg\}$ sparse view synthesis using gaussian splatting. *arXiv preprint arXiv:2312.00206*, 2023. 3

[44] Dejia Xu, Yifan Jiang, Peihao Wang, Zhiwen Fan, Humphrey Shi, and Zhangyang Wang. Sinnerf: Training neural radiance fields on complex scenes from a single image. In *European Conference on Computer Vision*, pages 736–753. Springer, 2022. 3

[45] Haofei Xu, Songyou Peng, Fangjinhua Wang, Hermann Blum, Daniel Barath, Andreas Geiger, and Marc Pollefeys. Depthsplat: Connecting gaussian splatting and depth. *arXiv preprint arXiv:2410.13862*, 2024. 2

[46] Qiangeng Xu, Zexiang Xu, Julien Philip, Sai Bi, Zhixin Shu, Kalyan Sunkavalli, and Ulrich Neumann. Point-nerf: Point-based neural radiance fields. In *Proceedings of the IEEE/CVF conference on computer vision and pattern recognition*, pages 5438–5448, 2022. 2

[47] Jiawei Yang, Marco Pavone, and Yue Wang. Freenerf: Improving few-shot neural rendering with free frequency regularization. In *Proceedings of the IEEE/CVF Conference on Computer Vision and Pattern Recognition*, pages 8254–8263, 2023. 2, 3

[48] Botao Ye, Sifei Liu, Haofei Xu, Xuetong Li, Marc Pollefeys, Ming-Hsuan Yang, and Songyou Peng. No pose, no problem: Surprisingly simple 3d gaussian splats from sparse unposed images. *arXiv preprint arXiv:2410.24207*, 2024. 2

[49] Alex Yu, Vickie Ye, Matthew Tancik, and Angjoo Kanazawa. pixelnerf: Neural radiance fields from one or few images. In *Proceedings of the IEEE/CVF Conference on Computer Vision and Pattern Recognition*, pages 4578–4587, 2021. 3

[50] Xianggang Yu, Mutian Xu, Yidan Zhang, Haolin Liu, Chongjie Ye, Yushuang Wu, Zizheng Yan, Chenming Zhu, Zhangyang Xiong, Tianyou Liang, et al. Mvimgnet: A large-scale dataset of multi-view images. In *Proceedings of the IEEE/CVF conference on computer vision and pattern recognition*, pages 9150–9161, 2023. 2, 5, A12

- [51] Zehao Yu, Anpei Chen, Binbin Huang, Torsten Sattler, and Andreas Geiger. Mip-splatting: Alias-free 3d gaussian splatting. In *Proceedings of the IEEE/CVF Conference on Computer Vision and Pattern Recognition*, pages 19447–19456, 2024. [2](#)
- [52] Zehao Yu, Torsten Sattler, and Andreas Geiger. Gaussian opacity fields: Efficient and compact surface reconstruction in unbounded scenes. *arXiv preprint arXiv:2404.10772*, 2024. [2](#)
- [53] Baowen Zhang, Chuan Fang, Rakesh Shrestha, Yixun Liang, Xiaoxiao Long, and Ping Tan. Rade-gs: Rasterizing depth in gaussian splatting. *arXiv preprint arXiv:2406.01467*, 2024. [2](#)
- [54] Richard Zhang, Phillip Isola, Alexei A Efros, Eli Shechtman, and Oliver Wang. The unreasonable effectiveness of deep features as a perceptual metric. In *Proceedings of the IEEE conference on computer vision and pattern recognition*, pages 586–595, 2018. [5](#)
- [55] Zehao Zhu, Zhiwen Fan, Yifan Jiang, and Zhangyang Wang. Fsgs: Real-time few-shot view synthesis using gaussian splatting. *arXiv preprint arXiv:2312.00451*, 2023. [2](#), [3](#), [6](#)
- [56] Chen Ziwen, Hao Tan, Kai Zhang, Sai Bi, Fujun Luan, Yicong Hong, Li Fuxin, and Zexiang Xu. Long-lrm: Long-sequence large reconstruction model for wide-coverage gaussian splats. *arXiv preprint arXiv:2410.12781*, 2024. [2](#)
- [57] Matthias Zwicker, Hanspeter Pfister, Jeroen Van Baar, and Markus Gross. Ewa volume splatting. In *Proceedings Visualization, 2001. VIS'01.*, pages 29–538. IEEE, 2001. [2](#)

A6. Details of Global Geometry Initialization

We provide additional details on the scaling process for pairwise-to-global alignment as discussed in Co-visible Global Geometry Initialization (Section 3.2 of the main draft).

Specifically, the geometric prior model, MAST3R, originally uses image pairs as input, requiring post-processing to align scales when more than two views are captured from the scene. This necessity arises because the predicted point maps are generated at varying scales. Such scale misalignment across independently computed relative poses introduces variance, leading to inaccuracies in camera pose estimation.

To integrate these pairwise pointmaps and camera information into a globally aligned geometry, we follow MAST3R [22] to construct a complete connectivity graph $\mathcal{G}(\mathcal{V}, \mathcal{E})$ of all the N input views, where the vertices \mathcal{V} and each edge $e = (n, m) \in \mathcal{E}$ indicate a shared visual content between images I_n and I_m . To convert the initially predicted point map $\{(\mathbf{P}_i \in \mathbb{R}^{H \times W \times 3})\}_{i=1}^N$ to be a globally aligned one $\{(\tilde{\mathbf{P}}_i \in \mathbb{R}^{H \times W \times 3})\}_{i=1}^N$, we update the point maps, transformation matrix, and a scale factor: For the complete graph, any image pair $e = (n, m) \in \mathcal{E}$, the point maps $\mathbf{P}_{n,n}, \mathbf{P}_{m,n}$ and confidence maps $\mathbf{O}_{n,n}, \mathbf{O}_{m,n}$. For clarity, let us define $\mathbf{P}_{n,e} := \mathbf{P}_{n,n}$, and $\mathbf{P}_{m,e} := \mathbf{P}_{m,n}$, $\mathbf{O}_{n,e} := \mathbf{O}_{n,n}$, and $\mathbf{O}_{m,e} := \mathbf{O}_{m,n}$. The optimization for the transformation matrix of edge \mathbf{T}_e , scaling factor σ_e and point map $\tilde{\mathbf{P}}$ are given by:

$$\tilde{\mathbf{P}}^* = \arg \min_{\tilde{\mathbf{P}}, \mathbf{T}, \sigma} \sum_{e \in \mathcal{E}} \sum_{v \in e} \sum_{i=1}^{HW} \mathbf{O}_{v,e}^i \left\| \tilde{\mathbf{P}}_v^i - \sigma_e \mathbf{T}_e \mathbf{P}_{v,e}^i \right\|. \quad (9)$$

Here, we slightly abuse notation and use $v \in e$ for $v \in \{n, m\}$ if $e = (n, m)$. The idea is that, for a given pair e , the same rigid transformation \mathbf{T}_e should align both pointmaps $\mathbf{P}_{n,e}$ and $\mathbf{P}_{m,e}$ with the world-coordinate pointmaps $\tilde{\mathbf{P}}_{n,e}$ and $\tilde{\mathbf{P}}_{m,e}$, since $\mathbf{P}_{n,e}$ and $\mathbf{P}_{m,e}$ are by definition both expressed in the same coordinate frame. To avoid the trivial optimum where $\sigma_e = 0, \forall e \in \mathcal{E}$, we enforce $\prod_e \sigma_e = 1$. Having aligned the point clouds, we commence the integration process by initializing 3D Gaussians [20], treating each point as a primitive. This post-processing step yields a globally aligned 3D Gaussians within only seconds, where inferring per-view point and confidence maps can be achieved real-time on a modern GPU.

A6.1. Additional Implementation Details.

We implement InstantSplat-2D-GS using the original 2D-GS CUDA kernel. All core components of our system are integrated into 2D-GS, including Focal Averaging, co-visible Global Geometry Initialization, Confidence-aware

Optimization, and Gaussian Bundle Adjustment. The optimization iterations are set to 1,500 for Gaussian training and 500 for aligning test view camera poses. Regularization for depth distortion and normal consistency begins at iterations 500 and 700, respectively.

A6.2. Evaluation on 2D-GS

In Table 6, we present the performance of InstantSplat-2D-GS on the tasks of novel view synthesis and multi-view stereo depth estimation using the Tanks and Temples dataset [21]. Following the train/test dataset split scheme described in the main draft, we sample 12 images for training and 12 for evaluation, covering the entire dataset. The test set contains 12 uniformly selected images (excluding first/last frames), with an equal number of training images sampled from remaining frames for sparse-view training. For novel view synthesis, we evaluate performance using PSNR, SSIM, and LPIPS. For depth estimation, we use the Absolute Relative Error (Rel) and Inlier Ratio (τ) with a threshold of 1.03 to assess each scene, following the approach of DUS3R [39]. We align the scene scale between the predictions and the ground truth, as our system does not depend on camera parameters for prediction. We normalize the predicted depth maps using the median of the predicted depths and similarly normalize the ground truth depths, which follows the procedures established in previous studies [33, 39] to ensure alignment between the predicted and ground truth depth maps. We use COLMAP [32] to perform dense stereo reconstruction on the entire video sequence, generating a high-quality multi-view stereo point cloud. The 3D dense points are then projected onto 2D image planes to create pseudo ground-truth depth maps for evaluation.

A7. More Experimental Results

A7.1. Additional Qualitative Results on the Benchmarks

We provide more visualized results and pose estimations on realistic outdoor scenes from the Tanks and Temples dataset [21] and MVIImgNet [50]. As shown in Fig.A9 and Fig.A10, InstantSplat consistently produces fewer artifacts than Gaussian-based methods (e.g., CF-3DGS [12]) and exhibits sharper details than NeRF-based methods (e.g., Nope-NeRF [5] and NeRFmm [41]).

A7.2. Video Demonstration

We provide free-viewpoint rendering on various in-the-wild datasets, including the **Sora** video, by uniformly sampling three frames from the entire video sequence. Additionally, we use stereo camera data from the **Perseverance Rover**, available on the [NASA website](#), and randomly sample three training views from the DL3DV-10K dataset [25].

As shown in Fig. A8 and Fig. A9, InstantSplat achieves accurate 3D reconstruction and high-quality novel view synthesis with as few as three training images, highlighting the robustness and effectiveness of our framework. As shown in Fig. A10, InstantSplat-2D-GS also achieves robust 3D surface reconstruction and high-quality novel view synthesis on in-the-wild data. For additional visualizations, please refer to our [instantsplat-webpage.zip](#) with opening the “index.html”.

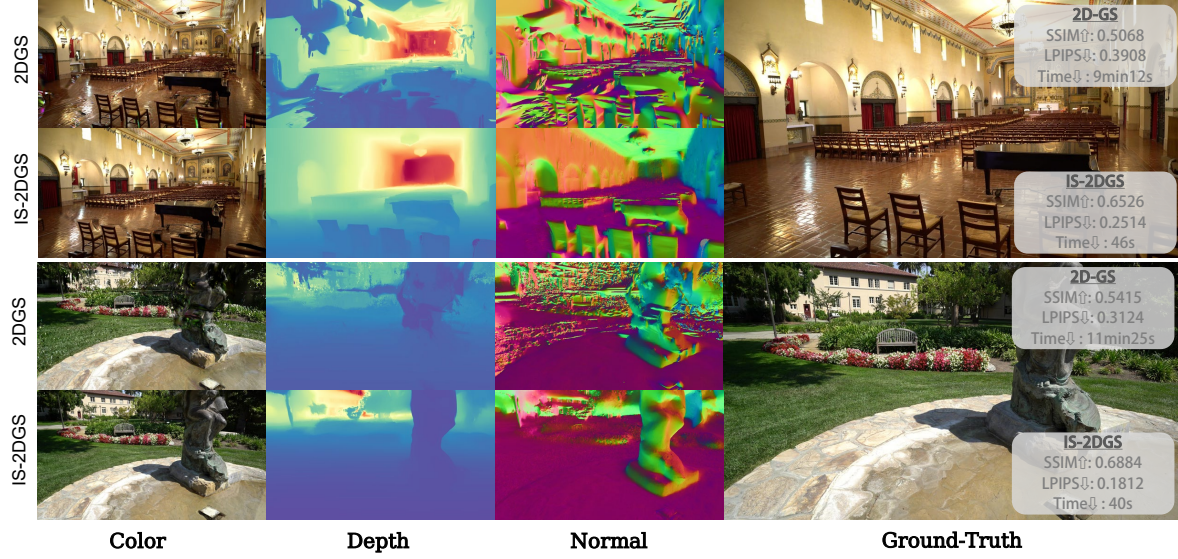


Figure A5. **Additional Visual Comparisons between 2D-GS and InstantSplat-2D-GS.** We present the rendering results of RGB images, depth maps, and normal maps from the Tanks and Temples dataset. The corresponding SSIM, LPIPS, and training time metrics are displayed on the right. Here, IS is used as an abbreviation for InstantSplat.

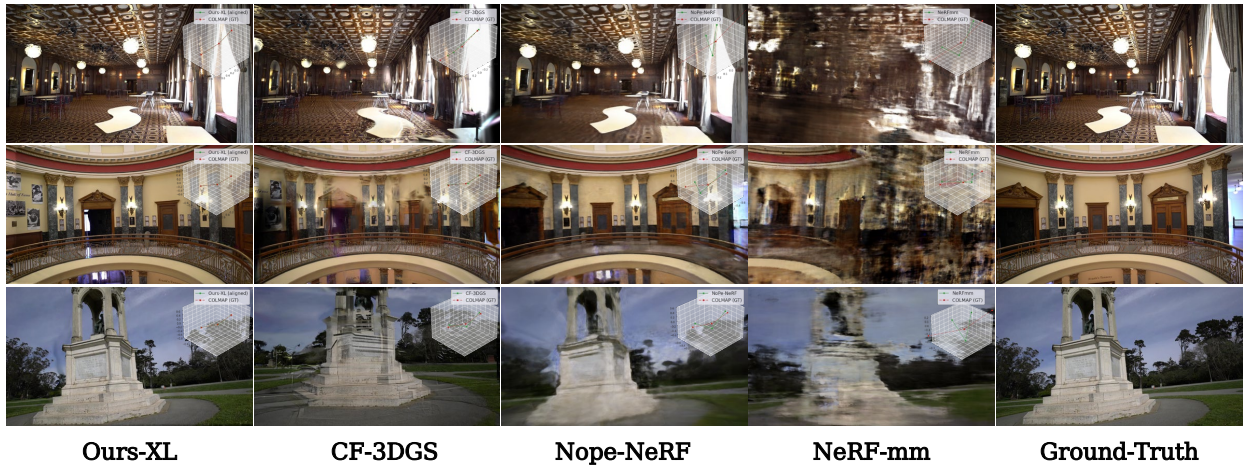


Figure A6. **Additional Visual Comparisons on the Tanks and Temples Dataset.** We present the rendering results from NeRFmm, Nope-NeRF, CF-3DGS, and Ours-XL.

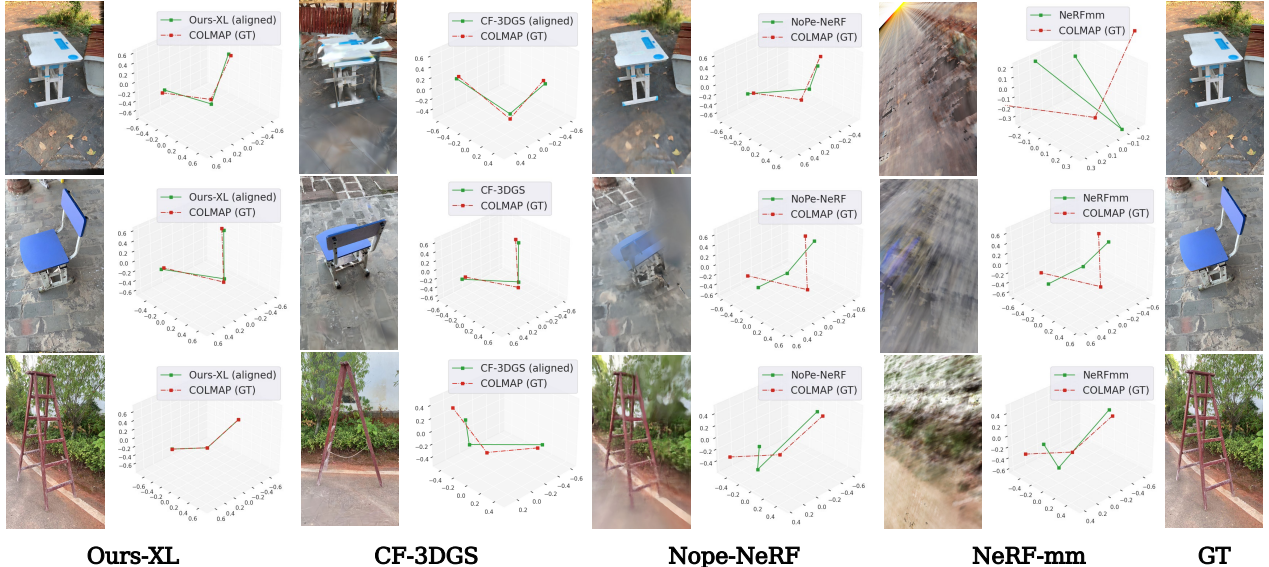


Figure A7. **Additional Visual Comparisons on the MVimgNet Dataset.** We present the rendering results from NeRF-mm, Nope-NeRF, CF-3DGS, and Ours-XL.



Figure A8. **Free-view Rendering on the Tanks and Temples Dataset.**

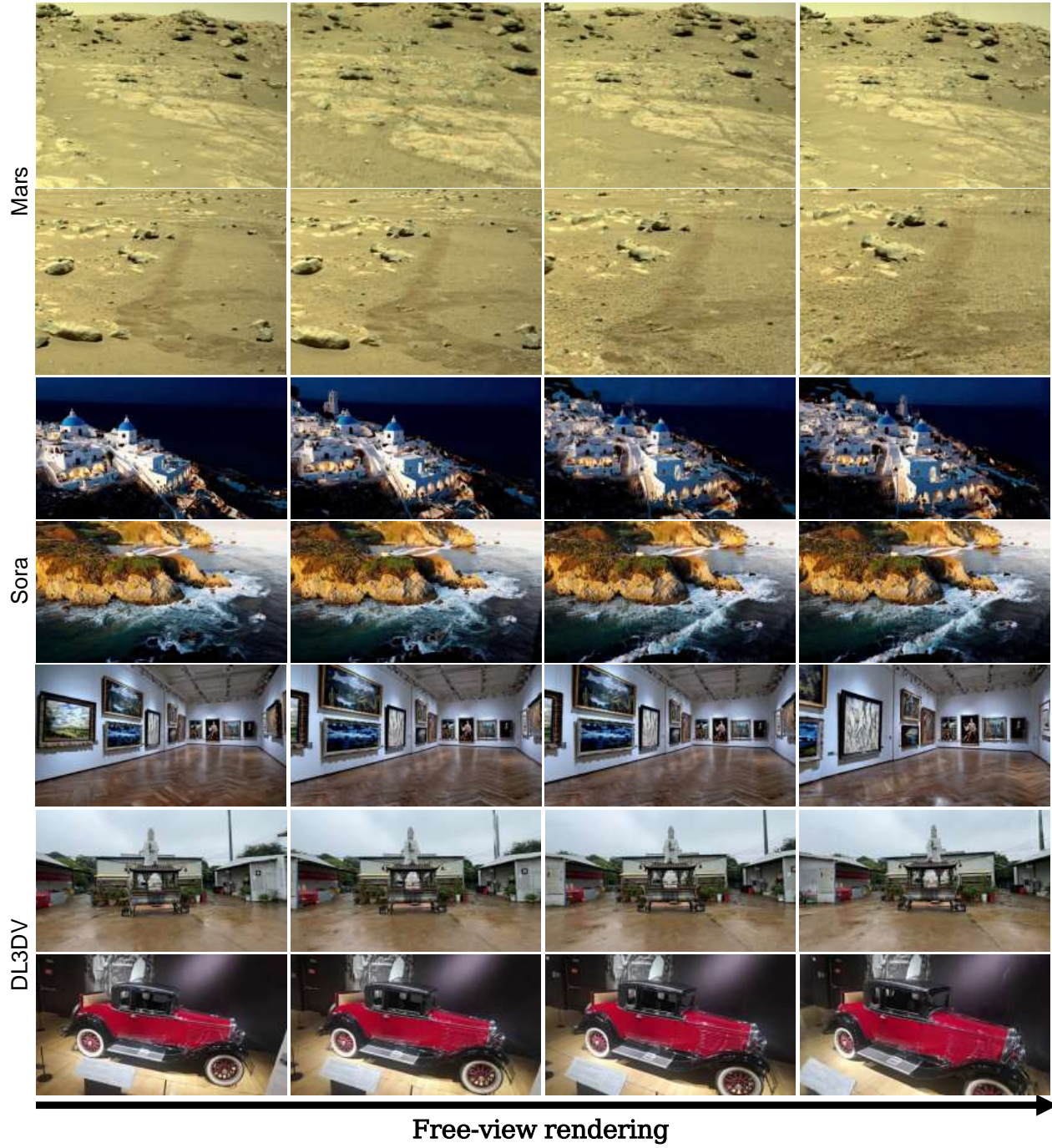


Figure A9. **Free-view Rendering on in-the-wild data.** We present the rendering results of three different in-the-wild data: Mars Rover Navigation, Sora Video and DL3DV-10K dataset.

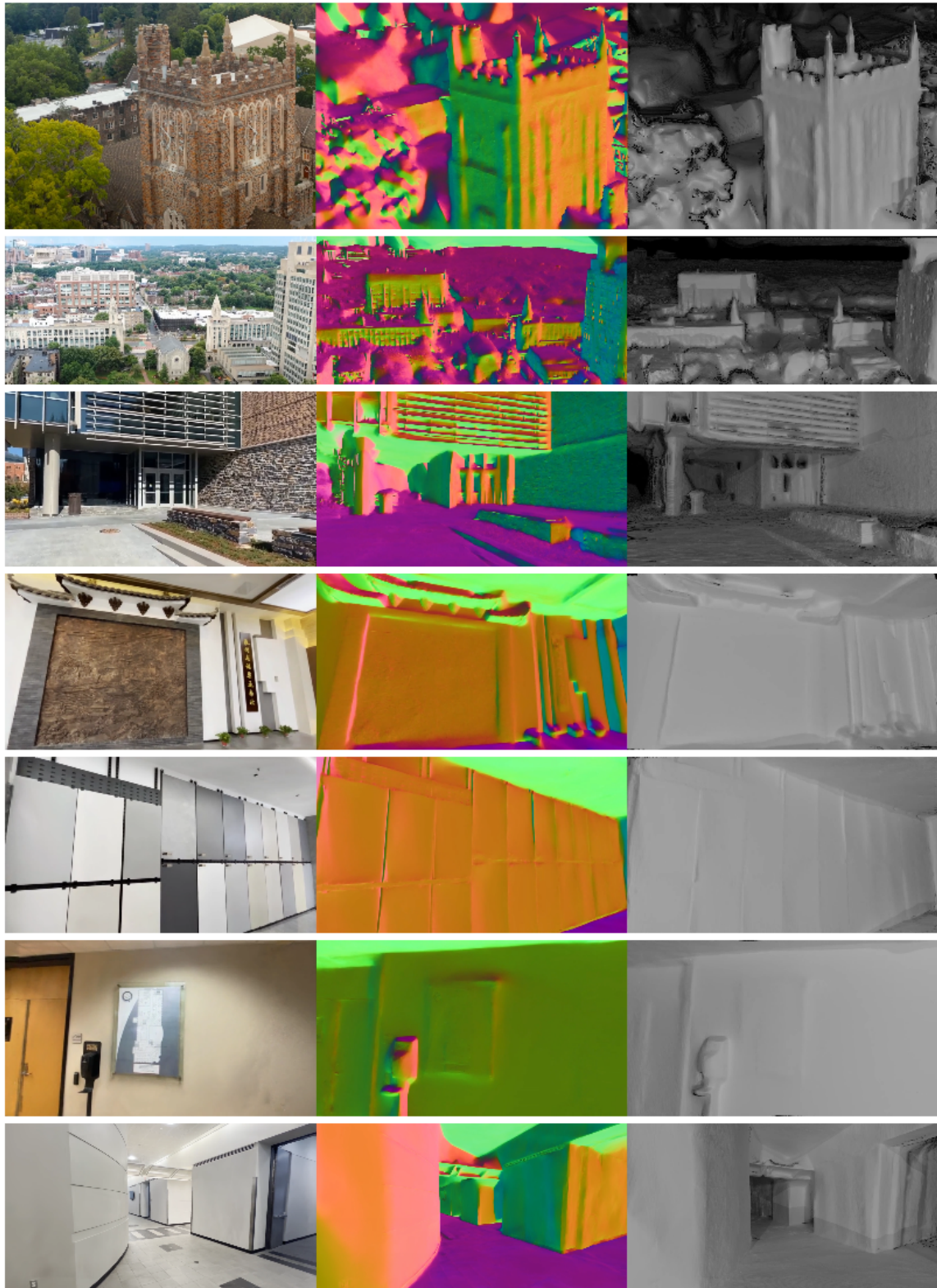


Figure A10. **Free-view Rendering of InstantSplat-2D-GS on in-the-wild data.** We present the rendering results of InstantSplat-2D-GS on in-the-wild data. Please refer to [instantsplat-webpage.zip](#) file for rendered video results.